Decoding the Broadband Emission of Two-Dimensional Pb-Sn Halide Perovskites through High-Throughput Exploration

Elham Foadian[1], Jonghee Yang[1]*, Yipeng Tang[1], Sumner B. Harris[2], Christopher M. Rouleau[2], Syed Joy[3], Kenneth R. Graham[3], Benjamin J. Lawrie[2,4], Bin Hu[1], Mahshid Ahmadi[1]*

[1] Institute for Advanced Materials and Manufacturing, Department of Materials Science and Engineering, University of Tennessee, Knoxville, TN 37996, United States.

[2] Center for Nanophase Materials Sciences, Oak Ridge National Laboratory, Oak Ridge, TN 37831, United States.

[3] Department of Chemistry, University of Kentucky, Lexington, KY 40506, United States.

[4] Materials Science and Technology Division, Oak Ridge National Laboratory, Oak Ridge, TN 37831, United States.

Corresponding authors:

* E-mails: jyang70@utk.edu, mahmadi3@utk.edu

Abstract

Unlike single-component two-dimensional (2D) metal halide perovskites (MHPs) exhibiting sharp excitonic photoluminescence (PL), a broadband PL emerges in mixed Pb-Sn 2D lattices. Two physical models –self-trapped exciton and defect-induced Stokes-shift – have been proposed to explain this unconventional phenomenon. However, both explanations provide limited rationalizations without consideration of the formidable compositional space, and thus, the fundamental origin of broadband PL remains elusive. Herein, we established our high-throughput automated experimental workflow to systematically explore the broadband PL in mixed Pb-Sn 2D MHPs, employing PEA (phenethylammonium) as a model cation known to work as a rigid organic spacer. Spectrally, the broadband PL becomes further broadened with rapid PEA_2PbI_4 phase segregation with increasing Pb concentrations during early-stage crystallization. Counterintuitively, MHPs with high Pb concentrations exhibit prolonged PL lifetimes despite high defect densities. Hyperspectral microscopy identifies substantial PEA_2PbI_4 phase segregation in those films, hypothesizing that the establishment of charge transfer excitons by the phase segregation upon crystallization is responsible for the extraordinary behavior; at high-Pb compositions, this far outperforms the leverage of defect-induced emission, thereby resulting in distinctive PL properties. Our high-throughput approach allows us to reconcile the controversial prior models describing the origin of the broadband emission in 2D Pb-Sn MHPs, shedding light on how to comprehensively explore the fundamentals and functionalities of the complex materials systems.

Introduction

The exceptional optical and electronic characteristics and affordability of metal hybrid perovskites (MHPs) have generated significant interest in the field of optoelectronic materials[1, 2]. In recent years, two-dimensional (2D) MHPs have gained notable attention for their immense promise in various optoelectronic applications, including solar cells and light-emitting diodes[3, 4]. Moreover, compared to 3D organic-inorganic halide perovskites, 2D MHPs offer a compelling advantage due to their unique quantum well structure which results in the efficient confinement of charge carriers within the inorganic layer and enhances their stability[5, 6]. Higher stability is a key factor that makes 2D structures a promising choice in various applications, ensuring better long-term performance and reliability[7-9].

A significant obstacle in advancing perovskite devices for widespread commercial use is the negative environmental impact due to the presence of toxic Pb[10, 11]. Among various elements considered as replacements for Pb^{2+}, Sn^{2+} stands out as the most promising candidate which shares similar ionic radius (112 and 120 pm for Sn^{2+} and Pb^{2+}, respectively[12, 13]) and electronic structures[14, 15]. Additionally, due to their closely matched elemental properties, Pb and Sn can be seamlessly integrated into a solid solution, forming a mixed Sn–Pb compound in any desired proportion[16]. Considering these compatibilities, the substituting of Pb with Sn in MHPs could be a significant step forward in addressing health and environmental concerns associated with Pb-based alternatives[17], and has led to extensive research aimed at developing environmentally friendly and sustainable MHP platforms[18, 19].

Interestingly, mixed Pb-Sn 2D perovskites differ from their 3D counterparts as their spectra are dominated by sub-bandgap broadband emissions rather than band-edge emissions, which still the origin of them remains a topic of debate and uncertainty[15]. The broad emission in mixed Pb-Sn 2D MHPs could potentially be attributed to self-trapped excitons (STEs)[20-23] or structural defects of the material, the latter hypothesizing that excitons become confined within the defect-induced sub-bandgap trap states and undergo radiative relaxation by Stokes shifts[20, 24, 25]. In this context, Li et al. claimed that Sn-doped PEA_2PbI_4 (PEA = Phenethylammonium) have a strong broadband emission which is attributed to Sn-triggered extrinsic STE[24]. On the other hand, Fang et al. found that the insensitivity of broadband emission to the Pb-Sn ratio and slower decay suggested defects, not exciton self-trapping, as the source of this emission in 2D Pb-Sn perovskite alloys[26, 27]. Meanwhile, Zhang et al. claimed that the broadband emission observed in PEA_2PbI_4/PEA_2SnI_4 double-layer heterostructures may be caused by charge transfer (CTE) emission at the PEA_2PbI_4:PEA_2SnI_4 interfaces[28].

So far, the broadband emission in 2D mixed Pb-Sn MHP systems has been mainly explored based on the physics perspective with the limited MHP compositions, relying on the understanding of exciton dynamics and lattice behaviors in such representative conditions. However, this approach conversely deters the understanding of the global spectral feature emerging in this compositional space. Furthermore, the lattice features and the resulting excitonic behaviors can also vary depending on the synthetic parameters, particularly responsible for the defects formation in this materials system[29]. Thus, the details in the broadband spectral evolution, where its control is important for some applications including white-light generation[30], as well as its genuine origin in 2D mixed Pb-Sn MHP system has not been comprehensively understood so far. Recently, high-throughput robotics synthesis platforms have introduced a fresh opportunity for investigating and enhancing materials processing techniques[31-34]. The lack of advanced tools

restricted progress in finding useful material combinations, therefore, it's crucial to emphasize the need for creating a high-throughput experimental approach to investigate various Pb-Sn combinations in 2D perovskite materials to understand the origin of their broadband emission, which hasn't been done yet.

Herein, we comprehensively explore the intriguing fundamental spectral behaviors in mixed Pb-Sn 2D MHPs by utilizing a high-throughput automated synthesis-characterization workflow. 2D MHP microcrystals with 96 different Pb-Sn ratios are synthesized in a microplate through combinatorial mixing of PEA_2PbI_4 and PEA_2SnI_4 precursors solution and subsequent crystallization. High-throughput optical characterization allows for efficient exploration of the serial changes of PL spectral features including the broadband emission as a function of Pb-Sn ratios over time, which cannot be expedited by human efforts.

We observe that the broadband emission globally emerges in every mixed-compositional range, and the spectral feature becomes further broadened with increasing Pb concentration. Also, phase separation of PEA_2PbI_4 from the mixed Pb-Sn 2D MHPs takes place over time in photoluminescence results, which is also facilitated with increasing Pb concentration. X-ray based chemical and structural analysis reveal that, counterintuitively, the amounts of defects (i.e., oxidized Sn^{4+}, metallic Sn; Sn^0, metallic Pb; Pb^0 and iodine vacancies) species are exponentially proportional to the Pb concentrations in the 2D MHPs, which is irrespective of the ambient exposure particularly in Pb-rich cases. This indicates that, for Pb-rich cases, those defects are inherently formed upon synthesis and not fully incorporated well into the inorganic lattice. Hyperspectral cathodoluminescence (CL) microscopy reveals the segregated PEA_2PbI_4 phase in those films as seen in early-stage crystallization behaviors evidenced by high-throughput observations. We hypothesize that the inherent, uncontrolled segregation of the PEA_2PbI_4 phase upon crystallization at high-Pb compositions establish charge transfer states dominant in the 2D MHP matrix, far outperforming the defect-induced emission – valid for the system with nominal Pb concentrations – and thereby resulting in PL broadening and longer lifetimes. Our high-throughput approach successfully resolves the prior controversies surrounding the origin of broadband emissions in 2D mixed Pb-Sn MHPs, offering a comprehensive understanding of the fundamental principles and practical applications of these intricate material systems.

Results and Discussion

High-throughput exploration of broadband emission in mixed Pb-Sn 2D MHPs

Essentially, the photophysics of materials are largely dependent on a multitude of factors having profound correlations with the crystallite lattice. Two distinctive factors, defects and phase separations, are known to substantially tune the emission features While extensive efforts have been made to control these obstacles in 3D metal halide perovskites, similar investigations for mixed Pb-Sn 2D MHPs, which possess nontrivial chemical complexity, have not been seriously considered.[35] Given these materials are synthesized via simple solution processing, comprehensive understanding of the crystallization dynamics is primarily necessary for exploration of the complex fundamental properties. Recently, we have successfully demonstrated that our high-throughput automated synthesis-characterization workflow provides systematic understanding of the early-stage crystallization dynamics of low-dimensional MHPs, allowing to gather fundamental insights into the functional materials systems[31].

Encouraged by this, to effectively explore the evolution of the broadband PL in a Pb-Sn compositional space of the 2D MHPs, we implement a high-throughput automated experimental workflow, as shown in **Figure 1**. By utilizing an automated pipetting robot, we systematically mix PEA_2PbI_4 and PEA_2SnI_4 precursor solutions with 96 different ratios in a microplate and subsequently synthesize the mixed Pb-Sn 2D MHP crystallites via antisolvent (e.g., toluene) injection within an hour (**Figure 1a** and **S1**)[31, 33, 34]. After mixing, the microplate is sealed and quickly transferred to an optical reader to characterize the PL properties of each binary composition of 2D MHP over time (for 1000 min). Monitoring of the PL changes over time provides us to insights into early-stage crystallization behaviors – difficult to be explored in conventional film fabrication process – of 2D MHPs in the Pb-Sn compositional space (**Figure 1b**), which primarily determine the defect densities and chemical inhomogeneities in the solution-processed materials associated with the broadband emission[31].
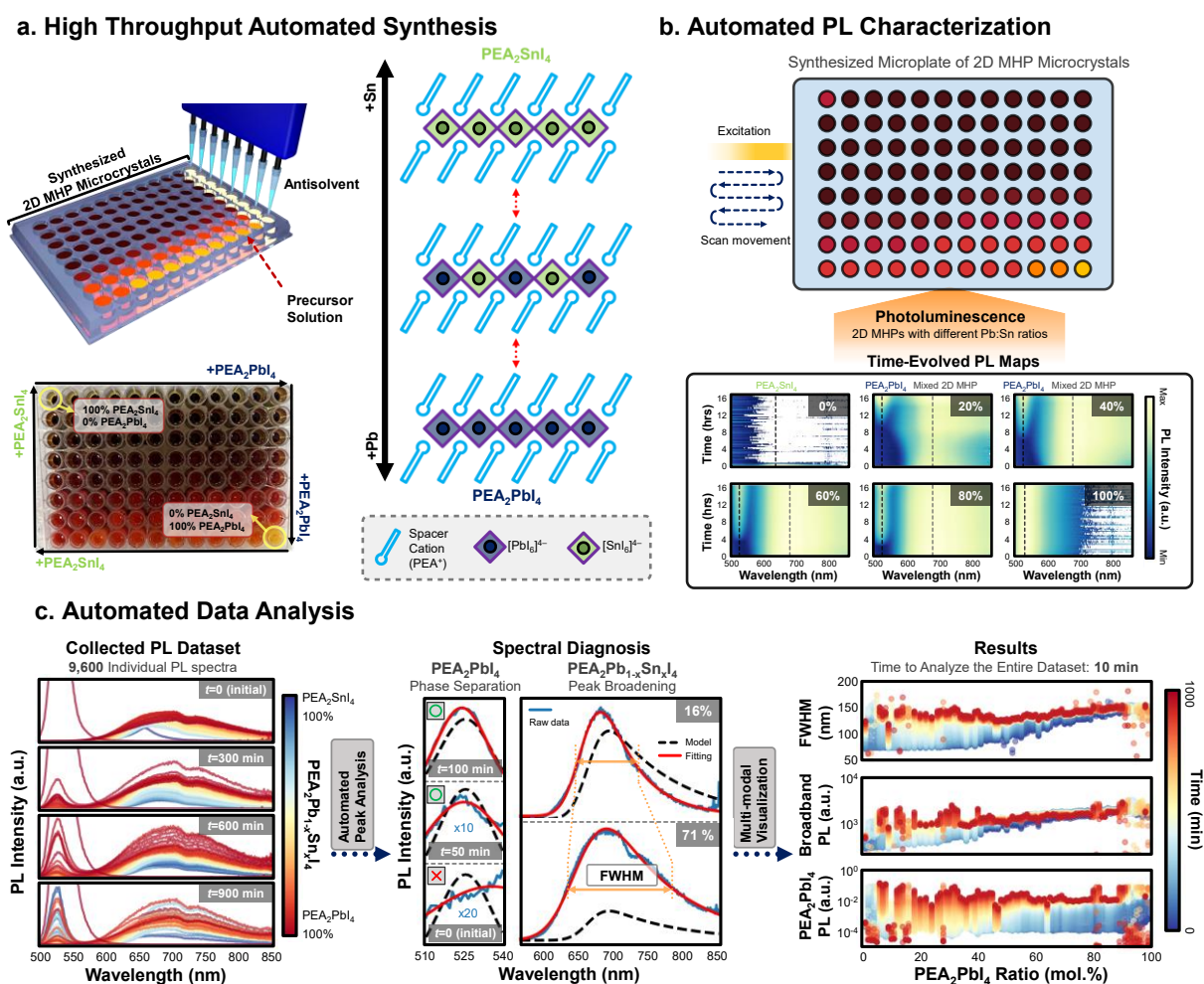

Figure 1. Experimental workflow showing the automated high-throughput exploration of 2D Pb-Sn MHPs. (a) High-throughput automated synthesis of the 2D MHP microcrystals via combinatorial mixing of PEA_2PbI_4 and PEA_2PbI_4 endmember precursors using pipetting robot and subsequent antisolvent (toluene) injection, allowing synthesis of 96 different binary mixtures. (b) High-throughput automated time-evolved PL characterizations using optical reader, providing 9,600 individual PL spectra for 1000 min. (c) Spectral diagnosis of PL dataset via implementation

of automated peak fitting function, allowing for comprehensive monitoring of PL characteristics for each composition over time. The total time to analyze the entire dataset takes only 10 min.

Practically, the time-evolved PL characterization produces 9600 individual PL spectra in a dataset (96 wells in a plate multiplied by 100 measurement cycles; **Figure S2**), which is impractical to be analyzed solely by human efforts. To address this challenge, a Python-based automated peak-fitting and tracking function is designed and implemented (**Figure 1c**)[31]. Here, we implement symmetric (Gaussian) and asymmetric (exponentially modified Gaussian) peak models for segregated PEA_2PbI_4 (*vide infra*) and broadband emissions, respectively. This peak-fitting function significantly streamlines the analysis of high-throughput observations, which automatically and accurately measures the PL properties including full-width at half-maximum (FWHM) and intensity for each peak component in the entire dataset within only 10 mins. As a result, the overall workflow allows for comprehensive and accelerated understanding of the crystallization dynamics in 2D MHPs across the Pb-Sn compositional space.
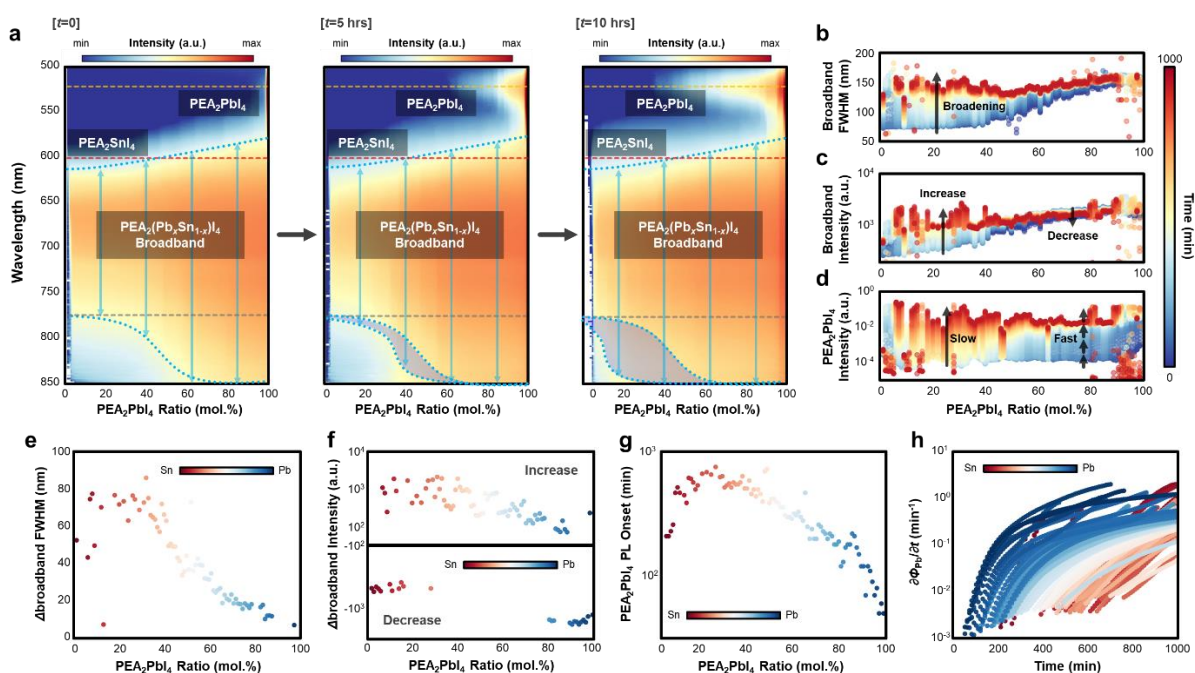

Figure 2. (a) 2D spectro-compositional maps of the mixed Pb-Sn 2D MHP microcrystals photoluminescence at three different timepoints across the compositional space, synthesized by high-throughput automated synthesis. (a) PL spectra as a function of PEA_2PbI_4 ratio at three different times. Temporal changes in (b) broadband FWHM, (c) broadband PL intensity, and (d) PEA_2PbI_4 PL intensity in the mixed Pb-Sn 2D MHP microcrystals across the Pb-Sn compositional space. Difference of (e) FWHM (ΔFWHM) and (f) broadband intensity (Δbroadband intensity) between the initial and final timepoints as a function of Pb compositional ratio. (g) The onset timepoints of PEA_2PbI_4 peak, and (h) 1st derivative of PEA_2PbI_4 PL intensity (corresponding to transient growth rates of PEA_2PbI_4 phase) as a function of Pb compositional ratio .

Figure 2a shows the PL spectral maps of the 2D MHP microcrystals across the Pb-Sn compositional space at three different timepoints: initial, 5 and 10 hours, respectively, showing a global trend in evolution of emission behaviors over time (corresponding overlays of PL spectra are shown in **Figure S3**). Except for pure PEA_2SnI_4 and PEA_2PbI_4 showing respective band-edge excitonic emission peaks at ~620 and ~525 nm, respectively (**Figure S4**)[20, 28, 36], initially, all mixed Pb-Sn 2D MHP microcrystals exhibit a broadband emission peaked at around 700 nm involving a shoulder at 750 nm. It is evident that an increase in the PEA_2PbI_4 ratio initially broadens the broadband emission, and as time progresses, the broad emission continues to widen – particularly at the low-Pb compositions (color-marked areas in the maps). Such dynamic changes suggest that there is an indirect relationship between the broadband features and Pb-Sn compositions; rather than the composition itself, it is likely that there are secondary factors associated with the peak broadening, the behaviors of which strongly depend on the Pb-Sn composition. Given the distinctive difference in PL intensity and stability between both endmembers (i.e., PEA_2SnI_4 and PEA_2PbI_4) respectively reflecting the defect formation rates and crystal growth (**Figure S4**),[37-39] the emergence of defects as consequences of incompatible chemical stability and crystallization rate can be responsible for the broadband feature in the mixed Pb-Sn MHP system. Indeed, defects in the lattice, particularly the iodine vacancy at apical direction, has been suggested to be the origin of the broadband emission[15, 40], which could be produced upon crystallization. On the other hand, these observations plausibly rule out the STE emission scenario, as the elastic distortion in lattice structure primarily depends on the Pb-Sn composition[26], which should be static upon crystallization.

Interestingly, an additional PEA_2PbI_4 PL is observed in the MHP microcrystals across the Pb-Sn compositional space over time, which initially emerges at high-Pb compositions and gradually expands to lower Pb compositions. This indicates that phase segregation of metal cations occurs during crystallization, and the rate of crystallization depends on the Pb-Sn compositions. To gain more detailed understanding on the PL behaviors in this materials system, we explore the time-evolved PL spectra of mixed Pb-Sn MHP microcrystals with selected compositional ratios, as visualized in **Figure S5**. Overall, two global features are observed: with increasing Pb composition ratios, (a) the initial broadband becomes wider, and (b) the emergence of PEA_2PbI_4 peaks becomes faster (from 600 to <100 min after antisolvent injection). We note that, specifically, the 2D MHP microcrystals with low Pb ratios (i.e., 10 to 40%) exhibit a sudden widening of the broadband – resembling the spectral shapes with comparable FWHM with the microcrystals with high Pb ratios – at respective timepoints, which qualitatively coincides with the time onset of the PEA_2PbI_4 PL emergence. This suggest a strong correlation between the broadband emission and the segregated PEA_2PbI_4 phase, which is plausible as the charge transfer state can be established between the segregated lattice and the mixed Pb-Sn 2D MHPs[28].

Through comprehensive analysis of PL dataset by implementation of peak-fitting function, the detailed parameters (i.e., broadband FWHM, evolutions of broadband and segregated PEA_2PbI_4 peak intensities) in time-evolved PL emissions are quantified across the Pb-Sn compositional space, as visualized in **Figure 2b-d**. Initially, the FWHM of broad emission expands from 60 nm to 170 nm with increasing Pb composition ratios from 1% to 99%. Such significant difference in FWHM suggests that the different mechanisms are associated with the emission behaviors of 2D mixed Pb-Sn MHPs at the low- and high-Pb compositional ranges. Also, the broadband continues to widen over 1000 mins as shown in **Figure 2b**. **Figure 2e** shows the difference in FWHM (ΔFWHM) between initial and final (after 1000 mins) as a function of Pb-Sn compositions, showing more pronounced peak broadening of ~80 nm in the MHPs with low-Pb compositional ratios over

time. As a result, the broadband FWHMs exhibit nominal values >120 nm across the entire compositional space, suggesting that the broadband emission mechanism at low-Pb 2D MHPs likely transforms to that of high-Pb counterparts.

Figure 2c shows the temporal evolution of broadband emission intensity across the Pb-Sn compositional space. Except for the MHPs with <20% Pb showing PL drops – as a result of rapid degradation by Sn oxidation (**Figure S4**)[36, 41, 42], for the MHPs with low-Pb compositions, intensity consistently increases (**Figure 2f**). Given the favorable oxidation and the consequent degradation of 2D Sn and low-Pb MHPs under ambient conditions, which promote defect formations over time, the temporal enhancements of broadband PL in low-Pb 2D MHPs seemingly support the scenario of defect-induced Stokes-shift contributing to broadband emission; The widening of the broadband in this compositional range also seems to align with this scenario. In contrast, for the MHPs with high-Pb compositions, an initial enhancement in broadband PL intensity is followed by a reduction. While such an up-and-down trend can be attributed to the competition between the slower crystallite growths and slower degradation – Pb^{2+} is more stable than Sn^{2+} upon ambient oxidation, the trend is irrespective of the continuous (though slow) widening of the broadband. In fact, not only the defects associated with broadband emission, the degradation of MHP crystallites also produces the defects promoting non-radiative recombination compromising PL intensity.[26] Given such a non-selectivity in defect formation upon degradation and inconsistency in PL trends at two distinctive Pb-Sn compositional ranges, it is likely that defect may not be the major factor contributing the widening of the broadband emission over time.

Now we focus on the segregation behavior of PEA_2PbI_4 peak across the compositional space. As shown in **Figure 2d**, notably faster PEA_2PbI_4 PL emergences are observed with increasing Pb composition ratios. From the intensity profiles, the onset timepoints of PEA_2PbI_4 peak are estimated across the compositional space (**Figure 2g**). Evidently, for the low-Pb compositions, the emergences of PEA_2PbI_4 peak first observed over several hundred minutes after antisolvent addition, whereas those of the MHPs with high-Pb compositions are detected within 100 minutes. These observations indicate that the segregation of PEA_2PbI_4 from the mixed Pb-Sn MHP phase becomes substantially accelerated with increasing Pb composition ratios. Note that the emergences of PEA_2SnI_4 is difficult to be identified and deconvoluted from the PL spectra, mainly due to the weak PLQY and the spectral proximity of the peak with the broadband[43]. In addition, considering the ambient-susceptible nature of Sn^{2+} leading to temporal degradation with substantial PL quenching via defect-induced non-radiative recombination, the contribution of PEA_2SnI_4 in the spectral feature of the 2D mixed Pb-Sn MHPs would be negligible. It is also noteworthy that the MHP microcrystals with <20% Pb compositions exhibit relatively faster PEA_2PbI_4 peak emergences compared with the nominal level of MHPs with intermediate Pb compositions. This can be explained by the rapid oxidation of Sn^{2+} in the inorganic lattice, which accelerates the uncontrollable phase changes upon degradation.

To deeply understand the kinetic aspects in PEA_2PbI_4 segregation, we take the first derivatives of PEA_2PbI_4 PL intensities with respect to the reaction time (i.e., $\partial\Phi_{Pb}/\partial t$) for the entire compositional space, as shown in **Figure 2f**. Notably faster growth rates of PEA_2PbI_4 (1-2 orders of magnitudes) are observed at the earlier timepoints (<200 minutes) for high-Pb 2D MHPs compared with the low-Pb counterparts. This indicates that, at the high-Pb compositions, the substantial phase segregation takes place at the very early-time during crystallization. In contrast, at the intermediate-Pb compositions, the rate of PEA_2PbI_4 segregation starts to slowly increase later after 200-600 minutes. Note that very small PL intensity of the segregated PEA_2PbI_4

crystallites below the detection limit of the instrument, attributed to their extremely small amounts, may not be collected during the measurement. However, the observed trends qualitatively suggest that phase separation takes place very initial dynamics, as evidenced by the large FWHMs of the broadband even at the initial PL spectra for Pb-rich MHP microcrystallites.

Overall, these results indicate that the segregation behavior of PEA_2PbI_4 phase in 2D mixed Pb-Sn MHPs becomes substantial with increasing Pb compositions. Inevitably, this can result in the non-trivial emergence of the segregated PEA_2PbI_4 phase during the crystallization of Sn-doped PEA_2PbI_4 thin films (*vide infra*) that have been prepared for photophysical investigations[15, 26, 40], which, surprisingly, has been somewhat overlooked from interpretation so far.

Note that the temporal evolutions for the PL parameters across the Pb-Sn compositional space share consistent trends with each other; gradually, the parameters undergo notable changes for the MHP microcrystals with low-Pb compositions, whereas those at high-Pb compositions show mild changes (or quickly reach to saturation level in PEA_2PbI_4 intensity) over time. Such distinctive features as a function of composition ratios strongly support our hypotheses that initially two different emission mechanisms – defect-induced Stokes shifts and establishment of CTE – dominates at each compositional range, while that governing at low-Pb compositions gradually transforms to the mechanism responsible for the 2D MHPs with high-Pb compositions. Additionally, given the strong correlations between the PL features and segregation behaviors of PEA_2PbI_4, we posit that the establishment of CTE states, rather than defects, is the majorly attributed to the broadband emission of high-Pb 2D MHPs.

Experimental characterization of mixed Pb-Sn 2D MHPs thin films

After high-throughput exploration of the crystallization behaviors in mixed Pb-Sn 2D MHPs, now we investigate the PL characteristics of the MHP films to understand how the early-stage crystallization behaviors influence to the chemical inhomogeneity and optical properties of the resulting films. Here, in addition to PEA_2SnI_4 and PEA_2PbI_4 endmembers, we select five mixed Pb-Sn compositions with serial increase of Pb compositional ratio (i.e., 10, 35, 60, 85, and 96%) and the corresponding 2D MHP films were prepared via spin coating. **Figure S6a** shows UV–vis absorption spectra of the films, showing serial blueshifts of the excitonic peak with increasing Pb compositional ratios. Note that the films with high-Pb ratios (i.e., 85 and 96%) exhibit distinctive excitonic peak of PEA_2PbI_4 separated from the corresponding absorption edge, which is not observed in Sn-rich films. This infers notable segregation action of PEA_2PbI_4 phase in the films at high-Pb ratios. From the corresponding Tauc plots, optical bandgap (E_g) of the mixed-phases are estimated and it reveals that the E_g of the films exhibits exponential increase from 1.94 to 2.35 eV with increasing Pb ratios (**Figure S6b and c**). The non-linear trend in E_g profile deviating from the Vegard's law could be attributed to the energy mismatch of the Pb 6s and Sn 5s states in the valence band[44, 45]. Additionally, significant phase segregation such as with the 85 and 96% samples can complicate the extraction of the bandgap and can explain the perceived deviation from Vegard's law since the absorbance would be a linear combination of the separate phases. We also estimated Urbach tail energy (E_u) in the film matrices[46], as shown in **Figure S6d**. Except for PEA_2PbI_4, gradual E_u increases from 280 to 380 meV are observed with increasing Pb ratios, indicating the qualitative increase of Pb higher energetic disorder at the band-tail states in the mixed Pb-Sn 2D MHPs[47, 48]. This could be attributed to the phase segregation and/or the defect densities formed in the films.

Figure S7a shows time-evolved PL spectra of mixed Pb-Sn 2D MHP thin films. Similar to the high-throughput observations, here the broadband emission becomes wider with increasing Pb composition ratios. Particularly, tiny but evident bumps of PEA_2PbI_4 emission at ~522 nm are also observed for the films with Pb composition ratios over 60%, which indeed confirms that phase segregation occurs upon the film crystallization at high Pb ratios. The emergence of PEA_2PbI_4 is not appreciable in the film with 10 and 35% Pb ratios, suggesting that the retarded and slow segregation behaviors observed in solution phase are reflected as the suppression of the segregation at these range. Meanwhile, the overall broadband PL intensities are gradually decreased for all films, as a result of temporal degradation upon ambient exposure during PL characterization.

We implement the devised peak-fitting function to analyze the time-evolution PL features in the films, as shown in **Figure S7b-d**. In **Figure S7b** it is shown that the temporal changes in broadband FWHM for low-Pb films are negligible, far different from the dynamic changes observed in microcrystal system. Also, the FWHM values of the low-Pb 2D MHPs exhibit nominal values of ~80 nm, whereas those of high-Pb MHPs show distinctively large values of 120-180 nm. This indicates that the physico-chemical action associated with the widening of the broadband – hypothesized to be PEA_2PbI_4 segregation that establishing CTE states – shown in microcrystal analysis is suppressed in the low-Pb films. The retarded and slow PEA_2PbI_4 segregation shown in high-throughput results of low-Pb MHPs support this, as the ion movement is deemed to be restricted in the solid matrix compared to the situation corresponds to the microcrystals system in solution phase[31]. Stronger bond dissociation energy of Sn-I (234 kJ/mol) compared to that of Pb-I (197 kJ/mol) also support this. Meanwhile, the temporal drops of broadband PL intensity in all films, as a result of ambient degradation can be observed (**Figure S7c**)[49, 50]. Collectively with the constant FWHM despite the increase in defects by temporal degradation, these observations indicate that these defects are unlikely to be the cause of changes in the broadband features.

The PL intensity of the segregated PEA_2PbI_4 phase in the films over time directly corroborates that the negligible phase segregation in the low-Pb films, which is, in contrast, distinctive in the films with high Pb compositions with stronger PL (**Figure S7d**). Note that the PEA_2PbI_4 intensity profiles of the high-Pb films exhibit initial increases followed by decreases, qualitatively replicating the trend of the broadband FWHM in these films. It is also observed that as the Pb content in the films is increased, there is a corresponding increase in the intensity of PEA_2PbI_4 which is consistent with the observed trends in FWHM and peak broadening. Overall, the characteristics in time-evolved PL spectra of the films obviously suggest that phase segregation is the major factor in broadband emission in mixed Pb-Sn 2D MHPs.
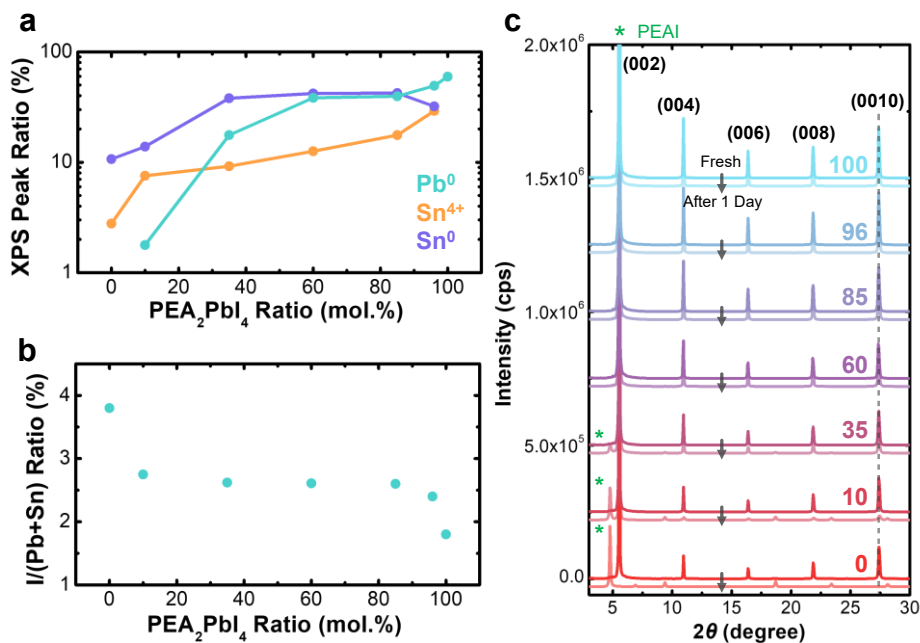
Figure 3. (a) Relative ratios of Pb^0, Sn^{4+} and Sn^0 with respect to total atomic contents. (b) Estimated I/(Pb+Sn) ratios of the 2D MHP films with different Pb ratios derived from the deconvolution of the corresponding XPS spectra. (c) XRD patterns of the freshly prepared 2D MHP films with different Pb ratios and those were left in ambient for one day. The green asterisks indicate the diffraction peak of PEAI.

To gain insights into the chemical structures of the elements, particularly the emergence of defects, across the compositional space in mixed Pb-Sn 2D MHP system, X-ray photoelectron spectroscopy (XPS) is conducted to the thin films and the Sn 3d, Pb 4f, and I 3d core-level photoelectron emission spectra of the films are collected. The baseline-subtracted Sn 3d XPS spectra are shown in **Figure S8a**. Two distinctive peaks centered at around 484.5 and 486 eV, assigned to be metallic Sn (Sn^0) and Sn^{2+}, respectively[51-53], are observed from the Sn $3d_{5/2}$ spectra in overall compositional range except for pure PEA_2SnI_4. The peaks at ~486 eV show asymmetric features attributed to the defective Sn^{4+} component centered at ~487 eV. This is widely observed from Sn-based perovskite because of the susceptibility of Sn^{2+} upon oxidation[51-53]. While the lattice-occupying Sn^{2+} peak proportionally becomes weaker with increasing Pb composition ratios, Sn^0 peak – known to also promote non-radiative recombination as defect[54] – substantially evolves and increases to the comparable intensity with that of Sn^{2+}. To get quantified insights into the Sn chemistry in 2D Pb-Sn MHPs, the Sn $3d_{5/2}$ spectra are deconvoluted into three distinct components corresponding to Sn^{4+}, Sn^{2+}, and Sn^0, respectively, as shown in **Figure S8b** (detailed values are summarized in **Table S1**). Obviously, in addition to Sn^0, it is observed that Sn^{4+} component gradually evolves with increasing Pb composition ratio (**Figure 3a**). Note that the films are carefully transferred to ultra-high vacuum chamber for measurement with a minimized exposure to ambient conditions, as corroborated by nearly exclusive emergence of Sn^{2+} peak in XPS Sn 3d spectrum of pure PEA_2SnI_4 film. Thus, these results indicate that more oxidized species are inherently formed with increasing Pb ratio upon crystallization.

Similarly, strong metallic Pb (Pb^0) peak – centered at ~136.5 eV in Pb $4f_{7/2}$ region – and the lattice-occupying Pb^{2+} peak (~137.8 eV in Pb $4f_{7/2}$ region) are observed in Pb 4f XPS spectra[55, 56], where the former component increases with increasing Pb composition ratio in Pb 4f XPS spectra (**Figure S9a**). The quantitative trend after peak deconvolution (see **Figure S9b** and **Table S1**) is also visualized in **Figure 3a**, clearly showing progressive increase of Pb^0 defects with increasing Pb ratio in the 2D MHP films. In contrast to PEA_2SnI_4, pure PEA_2PbI_4 film exhibits the strongest Pb^0 peak, suggesting that the origin of Sn^0 in mixed Pb-Sn MHPs is associated with the chemical action of Pb. Accordingly, exposure of Pb-based MHPs to UHV conditions and X-ray photon irradiation can cause iodine evaporation as a form of I_2 gas[51], thereby promoting Pb^{2+} to Pb^0 reduction[57, 58]. In mixed Pb-Sn 2D MHP, this reducing action – initiated from Pb-I part – can also effect on neighboring Sn^{2+} in the lattice, thereby producing Sn^0. In fact, it remains elusive whether these metallic species are inherently formed upon film crystallization or evolved upon UHV exposure. However, given that such reactions are deemed to be initiated primarily at the reactive and defective surface, these results suggest that the defect densities in the 2D MHP films are proportional to Pb ratios in the matrix, as also evidenced by E_u profiles for mixed Pb-Sn 2D MHPs.

Figure S10 shows I 3d spectra of the 2D MHP films, exhibiting serial upshifts in binding energy up to ~0.2 eV with increasing Pb ratio. In fact, stronger interaction between Sn and I compared with Pb counterpart is deemed to result in binding energy downshift with increasing Pb ratio, which is inconsistent with the observation. Such contradictory results infer that other factors are likely associated with the spectral feature. We estimated the I/(Pb+Sn) ratio of the films (**Figure 3b** and **Table S1**)[59], showing drop in I concentration in the 2D MHP matrix with increasing Pb ratio. That is, relatively higher density of I vacancies are formed in the film with increasing Pb ratios – particularly in high-Pb films, which is likely responsible for the upshifts in I 3d spectra. Note that among various defects, I vacancy, particularly that in equatorial position rather than in apical position, is known to responsible for local trapping of charge carrier and the consequent peak broadening in 2D Pb-Sn MHPs[15]. However, while the distinctive serial increase in the FWHM of the broadband is observed with increasing Pb ratio, the magnitude of increase in I vacancies – particularly in the mixed Pb-Sn 2D MHPs – is in the nominal level. This suggests that, while the larger amounts of defects are formed with increasing Pb ratios, the defects are not likely associated with the broadband emission in the mixed Pb-Sn 2D MHPs.

Through ultraviolet photoelectron spectroscopy (UPS) analysis, we observe distinctive changes in electronic structures of mixed Pb-Sn 2D MHPs as a function of Pb composition ratios (**Figure S11**). Here, a low-energy incidence photon of 10.2 eV was used as UV source to mitigate the beam-induced damage particularly on the organic part during experiments[60]. Based on the extracted Fermi energy (E_F) and valence band maximum (E_V) – respectively calculated from the secondary electron cut-off and valence band spectral regions (**Figure S12 and S13**) – and E_g of mixed-phases calculated from Tauc plots (**Figure S6**), the energy level diagram of the 2D MHP films are reconstructed (**Figure S14**). Overall, the E_F upshifts away from the valence band edge towards the middle of the E_g, indicating less p-type doping, are observed with increasing the Pb ratios, which aligns with the self p-doped nature of Sn rich MHPs[61]. The notable separation of the less p-typed PEA_2PbI_4 from the mixed Pb-Sn phases is likely reflected in the notable jump of E_F-E_V (from 0.67 to 0.84-0.89 eV) in the films with 85, 96, and 100% Pb. Also, tThe higher densities of iodine vacancies as evidenced in XPS analysis, which is known to facilitate a shift towards a more n-type surface character in three-dimensional MHP[62] – could be also associated with this jump. Summarizing, the interplay of self p-doping properties of Sn^{2+}, notable phase separation,

and higher densities of iodine vacancy synergistically bestow mediated p-type character to the films with increasing Pb ratios.

Defects are known to sacrifice stability of MHPs, suspecting that Pb-rich 2D Pb-Sn MHPs are more susceptible to degradation. To explore the influence of defects identified in XPS analysis on the stability of 2D MHP films, X-ray Diffraction (XRD) patterns of both the freshly prepared samples and those that were left in the ambient environment for a day are collected (**Figure 3c**). All films exhibit distinctive diffraction patterns of 2D MHPs with strong fundamental peaks at around 5.40°, assigned to be (002) face-on oriented lattice stacking mode[28]. After a day in ambient condition, with increasing Pb ratios, intensity drop of 2D MHP diffraction peaks as well as the emergence of new peak around 4.8° (marked with green asterisks; assigned to be PEAI[36, 63]) that shows stronger intensity with decreasing Pb ratios are observed. This indicates the 2D MHP crystallites, particularly the inorganic lattices are disintegrated upon ambient degradation. Note that the degradation is more facilitated in the film with decreasing Pb ratios due to the chemical lability of Sn^{2+} upon oxidation, which is proved to have smaller defect densities. These results suggest that the defect species identified in the XPS results are not responsible for the MHP stability. Moreover, this confirms that those defects are inherently formed during film crystallization rather than degradation.

To further investigate the role of defects on the PL characteristics, time-resolved PL decays of the 2D MHP films are measured using a sub-bandgap excitation wavelength of 1027 nm, as shown in **Figure 4a**. Here, as the photon energies below the bandgap lack the capacity to directly excite the carriers to the band edge, the broadband emission under this condition effectively negates STE emission scenario[40, 64]. While pure 2D MHPs exhibit very fast PL decays, interestingly, the mixed Pb-Sn MHPs exhibit slower decays, which are further prolonged with increasing Pb ratios. By employing a triexponential peak fitting model, the average lifetime is calculated for each sample (see **Table S2**). The pure 2D endmembers exhibit short lifetimes of 18 and 0.6 ns for PEA_2SnI_4 and PEA_2PbI_4, respectively, in good agreement with previous studies[26, 28]. Serial increases in PL lifetime from 20.62 to 275.06 ns are observed from the mixed Pb-Sn 2D MHPs with increasing Pb ratios, even though the non-radiative defect density becomes higher in the films in XPS observations[65, 66]. Such contradictory trend suggests that the broadband emission state is physically independent of the defects, ruling out the scenario of defect-induced Stoke-shifted broadband emission. Thus, these observations posit that the CTE emission mechanism dominates the broadband emission in mixed Pb-Sn 2D MHPs[28], which is plausible considering the observations of the segregated PEA_2PbI_4 phase in the films evidenced by optical characterizations (**Figure S6 and S7**).
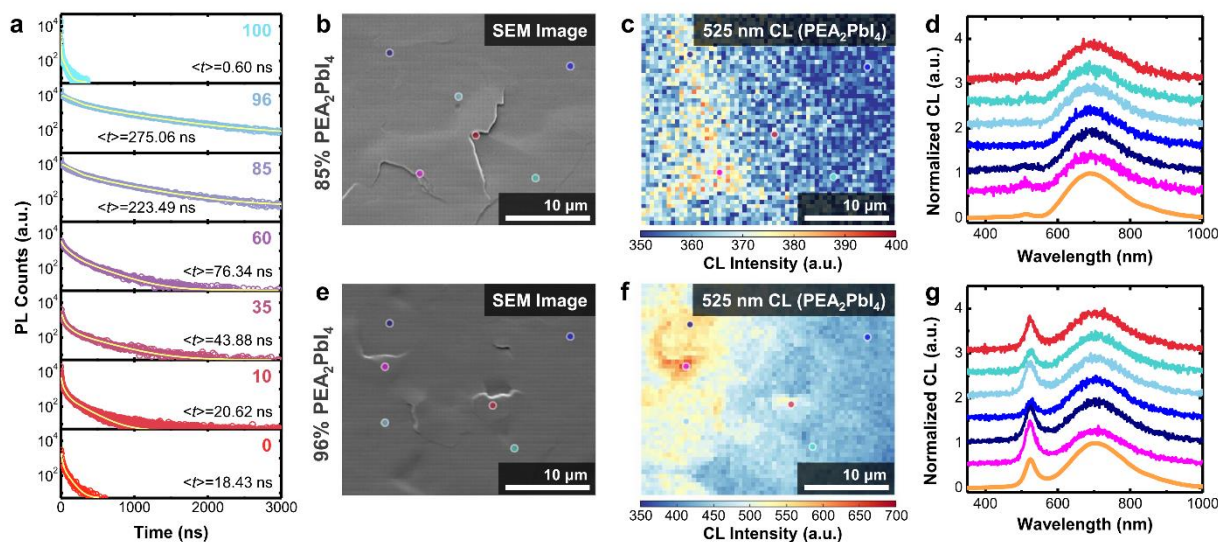
Figure 4. (a) PL decays and calculated average lifetimes collected from 2D MHP films with increasing Pb ratios. (b,e) SEM images, and (c,f) 525 nm-filtered CL maps (assigned to PEA_2PbI_4), and (d,g) local CL spectra of six spots color-marked on the maps for the films with 85 and 96% PEA_2PbI_4, respectively.

To gain spatially resolved insights into the mixed Pb-Sn 2D MHPs, hyperspectral cathodoluminescence (CL) microscopyis employed to several selected Pb-Sn thin films[35, 67, 68]. For pure PEA_2SnI_4 and PEA_2PbI_4 films, distinctive band-edge emissions (as visualized in 625 and 525 nm-filtered CL maps, respectively) of the films are observed across the entire surface with slight local intensity contrasts (**Figure S15**). This suggests that those films possess imperfect chemical homogeneity in the respective lattice interiors, likely attributed to the defects. Note that, in contrast to PEA_2PbI_4, substantial amounts of small voids are observed on the PEA_2SnI_4 surface. This could be explained by the extreme susceptibility of Sn^{2+}-based lattice upon ambient oxidation that leads to degradation[69], which however does not compromise the spectral shape of emission characteristics. That is, the formation of Sn^{4+} species upon oxidation is not relevant to the broadband PL features.

For mixed 2D Pb-Sn MHP films with low Pb ratios (i.e., 10, 35, and 60% PEA_2PbI_4), such voids are not observed on the surfaces, suggesting the oxidative degradation action is somewhat mitigated upon Pb incorporation (**Figure S16**). Also, in both 625 and 700 nm-filtered CL maps – corresponding with the peak and shoulder of the broadband spectra, broadband CL peak is observed across the entire film surface. Stronger CL intensities are observed along the grain boundaries, which could be attributed to the higher charge density at the edge of the 2D MHPs[70] that constitutes the grain boundaries. Specifically for the film with 35% PEA_2PbI_4, two spots within 500 nm pixel size emitting asymmetric CL emission centered around 388 nm are identified (**Figure S17**). This is likely attributed to the formation of SnO_2 particle as a product of Sn^{2+} to Sn^{4+} oxidation[71, 72]. Note that these spots are observed at the grain boundaries, suggesting that the oxidation action directly through the PEA-coordinated 2D faces is mitigated upon Pb incorporation and thereby exclusively occurring at the reactive surface spots.
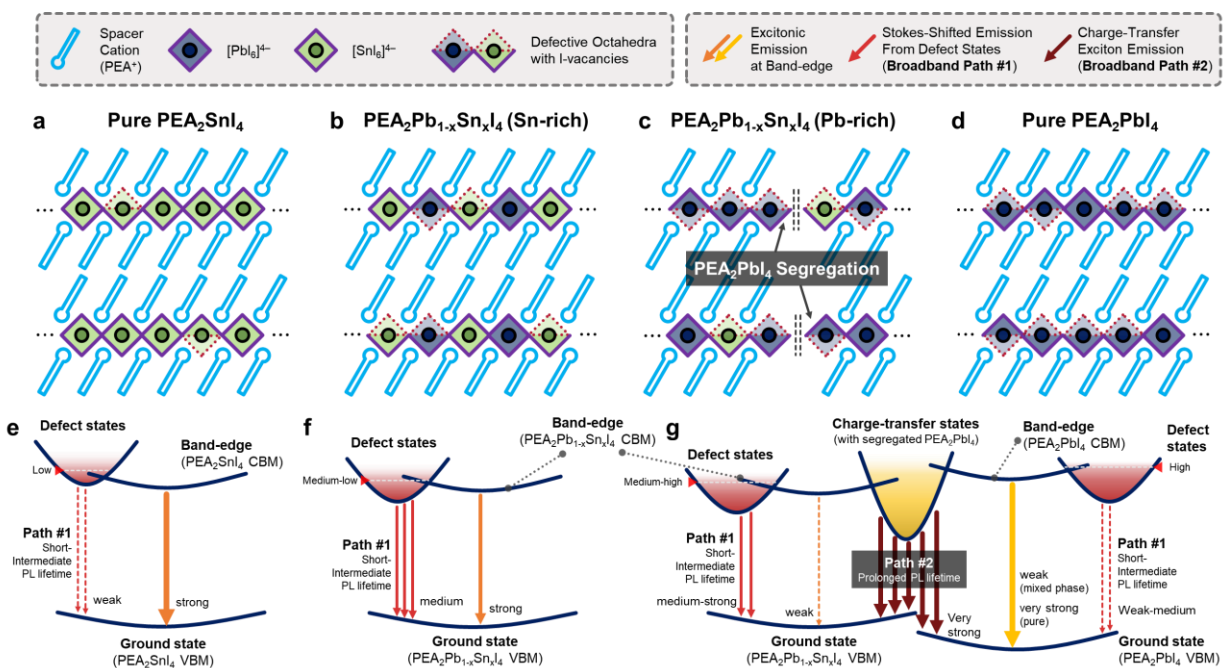
Figure 5. (a-d) Schematics describing lattice structures in 2D Pb-Sn MHPs and (e-g) corresponding Jablonski diagrams explaining broadband emission mechanisms at respective composition ranges.

Figure 4b and **4e** exhibit SEM images of mixed Pb-Sn 2D MHPs with high Pb ratios of 80 and 95%, respectively, showing nominal surface morphologies with flatten surface observed in the other films. 700 nm-filtered CL maps of the film also exhibit no specific spatial contrast in broadband emissions (**Figure S18**). However, 525 nm-filtered maps – responsible for PEA_2PbI_4 – clearly show non-zero CL intensity with distinctive local contrasts in these film surfaces, which exhibits the strongest intensities at the grain boundaries and then propagates towards the surroundings (**Figure 4c** and **4f**). This suggests that the PEA_2PbI_4 phase starts to segregate from the defective grain boundaries upon film crystallization and exhibit long-range coverage to the entire film surface. The emergence of the segregated PEA_2PbI_4 phase is also evident in the corresponding local CL spectra (**Figure 4d** and **4g**). Based on the results, we conclude that the interfacial contact between the segregated PEA_2PbI_4 lattice and the mixed Pb-Sn 2D MHP lattice effectively establishes CTE states across the entire film surface, thus majorly contributing to the long-lived broadband emission[28].

In fact, defects – particularly the iodine vacancy – have been claimed to promote peak widenings in broadband emission stemming from Stokes-shift (**Figure 5a, 5d and 5e**), which have been experimentally observed in PL spectra of the pure 2D MHPs collected at cryogenic temperatures[15, 25-27]. This model can be expanded to the observations in 2D MHPs with low-Pb ratios, which shows nominal level of the broadband FWHM but no appreciable segregated PEA_2PbI_4 phase (**Figure 5b** and **5f**). However, the nominal density levels of the iodine vacancies in the 2D MHP film matrix across the Pb-Sn compositional space, as evidenced in our XPS observations, cannot fully describe the strong broadband emissions with much wider peak FWHM in the 2D MHPs with high-Pb ratios that are clearly visible at room temperature. The longer PL

lifetimes of the 2D MHPs with high-Pb ratios despite the prominence of non-radiative defect densities (i.e., Pb^0, Sn^0, and Sn^{4+}) also corroborates that the defect-induced broadband emission model is not compatible with the actual phenomena. In this study, clearly, the emergence of PEA_2PbI_4 phase in the mixed Pb-Sn 2D MHP is spatially resolved, which reveals that the segregation action starts to occur at the grain boundaries that are deemed to possess larger amounts of defects. As hypothesized from the high-throughput observations, the incompatible crystallization kinetics with different chemical nature of Sn and Pb-based 2D MHPs could be mainly responsible for the formation of defects during the initial stage of crystallization of the solution-processed films. These defects, rather than inducing spectral Stokes-shift, in turn, can simultaneously promote the segregation of PEA_2PbI_4 during the rest of crystallization process. As a result, the "unexpected" interfacial contacts between PEA_2PbI_4 and the mixed Pb-Sn 2D MHPs establish the CTE states for broadband emission, which is independent of the defect states (**Figure 5c and 5g**). We stress that high-throughput exploration provides indispensable and comprehensive insights into the detailed early-stage crystallization dynamics that cannot easily be captured in conventional experimental workflow, significantly accelerating the discovery of the genuine origin of the fundamental materials properties. This work exemplifies how high-throughput automated experimental workflow sheds light on the fundamental discovery of functional materials.

Outlook

In summary, the early-stage crystallization dynamics of mixed Pb-Sn 2D MHPs are investigated by implementing high-throughput automated experimental workflow to explore the broadband PL emission of this materials system. This significantly accelerates the quantitative and comprehensive understanding of relationship between the broadband emission and crystallization behaviors, which has not been deeply considered so far. It is revealed that the broadband emission exhibits strong correlation with the segregation of PEA_2PbI_4 that is facilitated at high-Pb compositional ratios, hypothesizing that the establishment of CTE states are mainly responsible for the broadband emission. This is attributed to the incompatible crystallization kinetics and different chemical nature between Sn and Pb-based 2D MHPs, bestowing nontrivial chemical complexity in the film crystallites. XPS characterizations reveal that the overall defect densities progressively evolve with increasing Pb ratios, whereas the iodine vacancy – exclusively responsible for sub-bandgap states inducing Stokes-shift, remains insignificant variation across the mixed Pb-Sn compositional space. The serial increases of the prolonged broadband PL lifetimes with increasing Pb ratio despite larger densities of non-radiative defects strongly suggest that the electronic state of the broadband emission is physically independent of defect-induced states. Hyperspectral CL microscopy reveals that substantial segregation of PEA_2PbI_4 phases in the mixed Pb-Sn 2D MHP films particularly with high-Pb ratios indeed, the evolution of which is initiated from the defective grain boundaries. Thus, we conclude that evolution of prolonged broadband PL is originated from the establishment of CTE between the mixed Pb-Sn 2D MHP and long-range segregated PEA_2PbI_4, where the segregation is promoted by the substantial defect densities at the grain boundaries formed during crystallization. This effectively reconciles the proposed models describing fundamental origin of the broadband emission, which are in debate. Elucidation of genuine origin of these fundamental properties of promising materials shed light on development of sustainable and ubiquitous applications. More importantly, this study evidently exemplifies how the fundamental properties in the chemically complex materials can be

comprehensively explored and discovered in accelerated manner via unconventional high-throughput automated experimental workflow.

Acknowledgements

References

(1) Huang, J.; Yuan, Y.; Shao, Y.; Yan, Y. Understanding the physical properties of hybrid perovskites for photovoltaic applications. *Nature Reviews Materials* **2017**, *2* (7). DOI: 10.1038/natrevmats.2017.42.

(2) Luo, J.; He, R.; Lai, H.; Chen, C.; Zhu, J.; Xu, Y.; Yao, F.; Ma, T.; Luo, Y.; Yi, Z.; et al. Improved Carrier Management via a Multifunctional Modifier for High-Quality Low-Bandgap Sn-Pb Perovskites and Efficient All-Perovskite Tandem Solar Cells. *Advanced Materials* **2023**, *35* (22), e2300352. DOI: 10.1002/adma.202300352 .

(3) Liang, C.; Gu, H.; Xia, Y.; Wang, Z.; Liu, X.; Xia, J.; Zuo, S.; Hu, Y.; Gao, X.; Hui, W. Two-dimensional Ruddlesden–Popper layered perovskite solar cells based on phase-pure thin films. *Nature Energy* **2021**, *6* (1), 38-45.

(4) Tsai, H.; Nie, W.; Blancon, J. C.; Stoumpos, C. C.; Soe, C. M. M.; Yoo, J.; Crochet, J.; Tretiak, S.; Even, J.; Sadhanala, A. Stable light-emitting diodes using phase-pure Ruddlesden–Popper layered perovskites. *Advanced materials* **2018**, *30* (6), 1704217.

(5) Leung, T. L.; Ahmad, I.; Syed, A. A.; Ng, A. M. C.; Popović, J.; Djurišić, A. B. Stability of 2D and quasi-2D perovskite materials and devices. *Communications Materials* **2022**, *3* (1), 63.

(6) Li, X.; Hoffman, J. M.; Kanatzidis, M. G. The 2D halide perovskite rulebook: how the spacer influences everything from the structure to optoelectronic device efficiency. *Chemical reviews* **2021**, *121* (4), 2230-2291.

(7) Deng, C.; Zhou, G.; Chen, D.; Zhao, J.; Wang, Y.; Liu, Q. Broadband Photoluminescence in 2D Organic–Inorganic Hybrid Perovskites: (C7H18N2)PbBr4 and (C9H22N2)PbBr4. *The Journal of Physical Chemistry Letters* **2020**, *11* (8), 2934-2940. DOI: 10.1021/acs.jpclett.0c00578.

(8) Mao, L.; Tsai, H.; Nie, W.; Ma, L.; Im, J.; Stoumpos, C. C.; Malliakas, C. D.; Hao, F.; Wasielewski, M. R.; Mohite, A. D.; Kanatzidis, M. G. Role of Organic Counterion in Lead- and Tin-Based Two-Dimensional Semiconducting Iodide Perovskites and Application in Planar Solar Cells. *Chemistry of Materials* **2016**, *28* (21), 7781-7792. DOI: 10.1021/acs.chemmater.6b03054.

(9) Wu, X.; Trinh, M. T.; Zhu, X. Y. Excitonic Many-Body Interactions in Two-Dimensional Lead Iodide Perovskite Quantum Wells. *The Journal of Physical Chemistry C* **2015**, *119* (26), 14714-14721. DOI: 10.1021/acs.jpcc.5b00148.

(10) Abate, A. Perovskite solar cells go lead free. *Joule* **2017**, *1* (4), 659-664.

(11) Xi, J.; Loi, M. A. The fascinating properties of tin-alloyed halide perovskites. *ACS Energy Letters* **2021**, *6* (5), 1803-1810.

(12) Yang, J.; Han, W.; Jiang, B.; Wang, C.; Sun, Y.; Zhang, H.; Shimanoe, K.; Sun, P.; Lu, G. Sn2+ doped NiO hollow nanofibers to improve triethylamine sensing characteristics through tuning oxygen defects. *Sensors and Actuators B: Chemical* **2023**, *387*, 133801.

(13) Mulyani, B.; Manullang, A. S. F. B.; Purwanti, A. D.; Anisa, R. F. Analysis of adsorption of adsorbent sugarcane bagasse activated charcoal in concentration variations of Pb2+ and Cu2+ metal mixture. In *AIP Conference Proceedings*, 2023; AIP Publishing: Vol. 2540.

(14) Hao, F.; Stoumpos, C. C.; Chang, R. P.; Kanatzidis, M. G. Anomalous band gap behavior in mixed Sn and Pb perovskites enables broadening of absorption spectrum in solar cells. *Journal of the American Chemical Society* **2014**, *136* (22), 8094-8099. DOI: 10.1021/ja5033259 From NLM PubMed-not-MEDLINE.

(15) Kahmann, S.; Meggiolaro, D.; Gregori, L.; Tekelenburg, E. K.; Pitaro, M.; Stranks, S. D.; De Angelis, F.; Loi, M. A. The Origin of Broad Emission in ⟨100⟩ Two-Dimensional Perovskites: Extrinsic vs Intrinsic Processes. *ACS Energy Letters* **2022**, *7* (12), 4232-4241. DOI: 10.1021/acsenergylett.2c02123 From NLM PubMed-not-MEDLINE.

(16) Yao, H.; Zhou, F.; Li, Z.; Ci, Z.; Ding, L.; Jin, Z. Strategies for improving the stability of tin-based perovskite (ASnX3) solar cells. *Advanced Science* **2020**, *7* (10), 1903540.

(17) Cao, J.; Yan, F. Recent progress in tin-based perovskite solar cells. *Energy & Environmental Science* **2021**, *14* (3), 1286-1325. DOI: 10.1039/d0ee04007j.

(18) Ray, A.; De Trizio, L.; Zito, J.; Infante, I.; Manna, L.; Abdelhady, A. L. Light emission from low-dimensional pb-free perovskite-related metal halide nanocrystals. *Advanced Optical Materials* **2023**, *11* (4), 2202005.

(19) Zhao, J.; Zhang, Z.; Li, G.; Aldamasy, M. H.; Li, M.; Abate, A. Dimensional tuning in lead-free Tin Halide perovskite for solar cells. *Advanced Energy Materials* **2023**, *13* (13), 2204233.

(20) Kahmann, S.; Tekelenburg, E. K.; Duim, H.; Kamminga, M. E.; Loi, M. A. Extrinsic nature of the broad photoluminescence in lead iodide-based Ruddlesden-Popper perovskites. *Nature Communications* **2020**, *11* (1), 2344. DOI: 10.1038/s41467-020-15970-x From NLM PubMed-not-MEDLINE.

(21) Benin, B. M.; Dirin, D. N.; Morad, V.; Worle, M.; Yakunin, S.; Raino, G.; Nazarenko, O.; Fischer, M.; Infante, I.; Kovalenko, M. V. Highly Emissive Self-Trapped Excitons in Fully Inorganic Zero-Dimensional Tin Halides. *Angewandte Chemie International Edition* **2018**, *57* (35), 11329-11333. DOI: 10.1002/anie.201806452 From NLM PubMed-not-MEDLINE.

(22) Mao, L.; Guo, P.; Kepenekian, M.; Hadar, I.; Katan, C.; Even, J.; Schaller, R. D.; Stoumpos, C. C.; Kanatzidis, M. G. Structural Diversity in White-Light-Emitting Hybrid Lead Bromide Perovskites. *Journal of the American Chemical Society* **2018**, *140* (40), 13078-13088. DOI: 10.1021/jacs.8b08691 From NLM PubMed-not-MEDLINE.

(23) Mao, L.; Wu, Y.; Stoumpos, C. C.; Wasielewski, M. R.; Kanatzidis, M. G. White-Light Emission and Structural Distortion in New Corrugated Two-Dimensional Lead Bromide Perovskites. *Journal of the American Chemical Society* **2017**, *139* (14), 5210-5215. DOI: 10.1021/jacs.7b01312 From NLM PubMed-not-MEDLINE.

(24) Li, J.; Wang, H.; Li, D. Self-trapped excitons in two-dimensional perovskites. *Front Optoelectron* **2020**, *13* (3), 225-234. DOI: 10.1007/s12200-020-1051-x From NLM PubMed-not-MEDLINE.

(25) Paritmongkol, W.; Powers, E. R.; Dahod, N. S.; Tisdale, W. A. Two Origins of Broadband Emission in Multilayered 2D Lead Iodide Perovskites. *The Journal of Physical Chemistry Letters* **2020**, *11* (20), 8565-8572. DOI: 10.1021/acs.jpclett.0c02214 From NLM PubMed-not-MEDLINE.

(26) Fang, H. H.; Tekelenburg, E. K.; Xue, H.; Kahmann, S.; Chen, L.; Adjokatse, S.; Brocks, G.; Tao, S.; Loi, M. A. Unraveling the Broadband Emission in Mixed Tin-Lead Layered Perovskites. *Advanced Optical Materials* **2023**, *11* (4), 2202038.

(27) Hu, H.; Liu, Y.; Xie, Z.; Xiao, Z.; Niu, G.; Tang, J. Observation of defect luminescence in 2D Dion–Jacobson perovskites. *Advanced Optical Materials* **2021**, *9* (24), 2101423.

(28) Zhang, J.; Zhu, X.; Wang, M.; Hu, B. Establishing charge-transfer excitons in 2D perovskite heterostructures. *Nature Communications* **2020**, *11* (1), 2618. DOI: 10.1038/s41467-020-16415-1 From NLM PubMed-not-MEDLINE.

(29) Zhang, C.; Lin, J. Defect-related luminescent materials: synthesis, emission properties and applications. *Chemical Society Reviews* **2012**, *41* (23), 7938-7961.

(30) Smith, M. D.; Karunadasa, H. I. White-light emission from layered halide perovskites. *Accounts of chemical research* **2018**, *51* (3), 619-627.

(31) Yang, J.; Lawrie, B. J.; Kalinin, S. V.; Ahmadi, M. High-Throughput Automated Exploration of Phase Growth Behaviors in Quasi-2D Formamidinium Metal Halide Perovskites. *Advanced Energy Materials* **2023**, *13* (43), 2302337.

(32) Sanchez, S. L.; Tang, Y.; Hu, B.; Yang, J.; Ahmadi, M. Understanding the ligand-assisted reprecipitation of CsPbBr3 nanocrystals via high-throughput robotic synthesis approach. *Matter* **2023**, *6* (9), 2900-2918.

(33) Higgins, K.; Valleti, S. M.; Ziatdinov, M.; Kalinin, S. V.; Ahmadi, M. Chemical Robotics Enabled Exploration of Stability in Multicomponent Lead Halide Perovskites via Machine Learning. *ACS Energy Letters* **2020**, *5* (11), 3426-3436. DOI: 10.1021/acsenergylett.0c01749.

(34) Higgins, K.; Ziatdinov, M.; Kalinin, S. V.; Ahmadi, M. High-Throughput Study of Antisolvents on the Stability of Multicomponent Metal Halide Perovskites through Robotics-Based Synthesis and Machine Learning Approaches. *Journal of the American Chemical Society* **2021**, *143* (47), 19945-19955. DOI: 10.1021/jacs.1c10045 From NLM PubMed-not-MEDLINE.

(35) Yang, J.; LaFollette, D. K.; Lawrie, B. J.; Ievlev, A. V.; Liu, Y.; Kelley, K. P.; Kalinin, S. V.; Correa-Baena, J.-P.; Ahmadi, M. Understanding the Role of Cesium on Chemical Complexity in Methylammonium-Free Metal Halide Perovskites. *Advanced Energy Materials* **2023**, *13* (33), 2202880.

(36) Ju, Y.; Wu, X. g.; Huang, S.; Dai, G.; Song, T.; Zhong, H. The Evolution of Photoluminescence Properties of PEA2SnI4 Upon Oxygen Exposure: Insight into Concentration Effects. *Advanced Functional Materials* **2022**, *32* (2), 2108296.

(37) Chen, Y.; Sun, Y.; Peng, J.; Chábera, P.; Honarfar, A.; Zheng, K.; Liang, Z. Composition Engineering in Two-Dimensional Pb–Sn-Alloyed Perovskites for Efficient and Stable Solar Cells. *ACS applied materials & interfaces* **2018**, *10* (25), 21343-21348.

(38) Wei, M.; Xiao, K.; Walters, G.; Lin, R.; Zhao, Y.; Saidaminov, M. I.; Todorović, P.; Johnston, A.; Huang, Z.; Chen, H. Combining efficiency and stability in mixed tin–lead perovskite solar cells by capping grains with an ultrathin 2D layer. *Advanced Materials* **2020**, *32* (12), 1907058.

(39) Wang, Z.; Ou, Q.; Zhang, Y.; Zhang, Q.; Hoh, H. Y.; Bao, Q. Degradation of two-dimensional CH3NH3PbI3 perovskite and CH3NH3PbI3/graphene heterostructure. *ACS applied materials & interfaces* **2018**, *10* (28), 24258-24265.

(40) Li, T.; Chen, X.; Wang, X.; Lu, H.; Yan, Y.; Beard, M. C.; Mitzi, D. B. Origin of broad-band emission and impact of structural dimensionality in tin-alloyed Ruddlesden–Popper hybrid lead iodide perovskites. *ACS Energy Letters* **2019**, *5* (2), 347-352.

(41) Smith, M. A.; Chen, M.; Dai, Z.; Antolini, C.; Jayasekara, G. K.; Yadavalli, S. K.; Reinhart, B. J.; Padture, N. P.; Hayes, D. Real-Time Investigation of Sn (II) Oxidation in Pb-Free Halide Perovskites by X-ray Absorption and Mössbauer Spectroscopy. *ACS Applied Energy Materials* **2021**, *4* (5), 4327-4332.

(42) Cheng, Y.-H.; Moriyama, R.; Ebe, H.; Mizuguchi, K.; Yamakado, R.; Nishitsuji, S.; Chiba, T.; Kido, J. Two-step crystallization for low-oxidation tin-based perovskite light-emitting diodes. *ACS Applied Materials & Interfaces* **2022**, *14* (20), 22941-22949.

(43) Vescio, G.; Sanchez-Diaz, J.; Frieiro, J. L.; Sanchez, R. S.; Hernandez, S.; Cirera, A.; Mora-Sero, I.; Garrido, B. 2D PEA$_2$SnI$_4$ Inkjet-Printed Halide Perovskite LEDs on Rigid and Flexible Substrates. *ACS Energy Letters* **2022**, *7* (10), 3653-3655. DOI: 10.1021/acsenergylett.2c01773.

(44) Underwood, C. C.; Carey, J. D.; Silva, S. R. P. Nonlinear Band Gap Dependence of Mixed Pb–Sn 2D Ruddlesden–Popper PEA2Pb1–x Sn x I4 Perovskites. *The Journal of Physical Chemistry Letters* **2021**, *12* (5), 1501-1506.

(45) Eperon, G. E.; Leijtens, T.; Bush, K. A.; Prasanna, R.; Green, T.; Wang, J. T.-W.; McMeekin, D. P.; Volonakis, G.; Milot, R. L.; May, R. Perovskite-perovskite tandem photovoltaics with optimized band gaps. *Science* **2016**, *354* (6314), 861-865.

(46) Urbach, F. The long-wavelength edge of photographic sensitivity and of the electronic absorption of solids. *Physical review* **1953**, *92* (5), 1324.

(47) Sadhanala, A.; Deschler, F.; Thomas, T. H.; Dutton, S. E.; Goedel, K. C.; Hanusch, F. C.; Lai, M. L.; Steiner, U.; Bein, T.; Docampo, P. Preparation of single-phase films of CH3NH3Pb (I1–x Br x) 3 with sharp optical band edges. *The Journal of Physical Chemistry Letters* **2014**, *5* (15), 2501-2505.

(48) Cody, G.; Tiedje, T.; Abeles, B.; Brooks, B.; Goldstein, Y. Disorder and the optical-absorption edge of hydrogenated amorphous silicon. *Physical Review Letters* **1981**, *47* (20), 1480.

(49) Fang, H. H.; Yang, J.; Tao, S.; Adjokatse, S.; Kamminga, M. E.; Ye, J.; Blake, G. R.; Even, J.; Loi, M. A. Unravelling light-induced degradation of layered perovskite crystals and Design of Efficient Encapsulation for improved Photostability. *Advanced Functional Materials* **2018**, *28* (21), 1800305.

(50) Lee, J.-W.; Dai, Z.; Han, T.-H.; Choi, C.; Chang, S.-Y.; Lee, S.-J.; De Marco, N.; Zhao, H.; Sun, P.; Huang, Y. 2D perovskite stabilized phase-pure formamidinium perovskite solar cells. *Nature communications* **2018**, *9* (1), 3021.

(51) Wieczorek, A.; Lai, H.; Pious, J.; Fu, F.; Siol, S. Resolving Oxidation States and X–site Composition of Sn Perovskites through Auger Parameter Analysis in XPS. *Advanced Materials Interfaces* **2023**, *10* (7), 2201828.

(52) Yeom, K. W.; Lee, D. K.; Park, N. G. Hard and Soft Acid and Base (HSAB) Engineering for Efficient and Stable Sn-Pb Perovskite Solar Cells. *Advanced Energy Materials* **2022**, *12* (48), 2202496.

(53) Lin, R.; Xu, J.; Wei, M.; Wang, Y.; Qin, Z.; Liu, Z.; Wu, J.; Xiao, K.; Chen, B.; Park, S. M. All-perovskite tandem solar cells with improved grain surface passivation. *Nature* **2022**, *603* (7899), 73-78.

(54) Song, T. B.; Yokoyama, T.; Stoumpos, C. C.; Logsdon, J.; Cao, D. H.; Wasielewski, M. R.; Aramaki, S.; Kanatzidis, M. G. Importance of Reducing Vapor Atmosphere in the Fabrication of Tin-Based Perovskite Solar Cells. *Journal of the American Chemical Society* **2017**, *139* (2), 836-842. DOI: 10.1021/jacs.6b10734.

(55) Bi, D.; Yi, C.; Luo, J.; Décoppet, J.-D.; Zhang, F.; Zakeeruddin, S. M.; Li, X.; Hagfeldt, A.; Grätzel, M. Polymer-templated nucleation and crystal growth of perovskite films for solar cells with efficiency greater than 21%. *Nature Energy* **2016**, *1* (10), 1-5.

(56) Zhuang, J.; Mao, P.; Luan, Y.; Yi, X.; Tu, Z.; Zhang, Y.; Yi, Y.; Wei, Y.; Chen, N.; Lin, T. Interfacial passivation for perovskite solar cells: the effects of the functional group in phenethylammonium iodide. *ACS Energy Letters* **2019**, *4* (12), 2913-2921.

(57) Liang, J.; Hu, X.; Wang, C.; Liang, C.; Chen, C.; Xiao, M.; Li, J.; Tao, C.; Xing, G.; Yu, R. Origins and influences of metallic lead in perovskite solar cells. *Joule* **2022**, *6* (4), 816-833.

(58) McGettrick, J. D.; Hooper, K.; Pockett, A.; Baker, J.; Troughton, J.; Carnie, M.; Watson, T. Sources of Pb (0) artefacts during XPS analysis of lead halide perovskites. *Materials Letters* **2019**, *251*, 98-101.

(59) Scofield, J. H. Hartree-Slater subshell photoionization cross-sections at 1254 and 1487 eV. *Journal of Electron Spectroscopy and Related Phenomena* **1976**, *8* (2), 129-137.

(60) Boehm, A. M.; Wieser, J.; Butrouna, K.; Graham, K. R. A new photon source for ultraviolet photoelectron spectroscopy of organic and other damage-prone materials. *Organic Electronics* **2017**, *41*, 9-16.

(61) Chung, I.; Song, J. H.; Im, J.; Androulakis, J.; Malliakas, C. D.; Li, H.; Freeman, A. J.; Kenney, J. T.; Kanatzidis, M. G. CsSnI3: Semiconductor or metal? High electrical conductivity and strong near-infrared photoluminescence from a single material. High hole mobility and phase-transitions. *Journal of the American Chemical Society* **2012**, *134* (20), 8579-8587. DOI: 10.1021/ja301539s.

(62) Wang, Q.; Shao, Y.; Xie, H.; Lyu, L.; Liu, X.; Gao, Y.; Huang, J. Qualifying composition dependent p and n self-doping in CH3NH3PbI3. *Applied Physics Letters* **2014**, *105* (16).

(63) Cho, K. T.; Grancini, G.; Lee, Y.; Oveisi, E.; Ryu, J.; Almora, O.; Tschumi, M.; Schouwink, P. A.; Seo, G.; Heo, S. Selective growth of layered perovskites for stable and efficient photovoltaics. *Energy & Environmental Science* **2018**, *11* (4), 952-959.

(64) Hu, T.; Smith, M. D.; Dohner, E. R.; Sher, M.-J.; Wu, X.; Trinh, M. T.; Fisher, A.; Corbett, J.; Zhu, X.-Y.; Karunadasa, H. I. Mechanism for broadband white-light emission from two-dimensional (110) hybrid perovskites. *The Journal of Physical Chemistry Letters* **2016**, *7* (12), 2258-2263.

(65) Parrott, E. S.; Milot, R. L.; Stergiopoulos, T.; Snaith, H. J.; Johnston, M. B.; Herz, L. M. Effect of structural phase transition on charge-carrier lifetimes and defects in CH3NH3SnI3 perovskite. *The Journal of Physical Chemistry Letters* **2016**, *7* (7), 1321-1326.

(66) de Quilettes, D. W.; Vorpahl, S. M.; Stranks, S. D.; Nagaoka, H.; Eperon, G. E.; Ziffer, M. E.; Snaith, H. J.; Ginger, D. S. Impact of microstructure on local carrier lifetime in perovskite solar cells. *Science* **2015**, *348* (6235), 683-686.

(67) Dou, L.; Wong, A. B.; Yu, Y.; Lai, M.; Kornienko, N.; Eaton, S. W.; Fu, A.; Bischak, C. G.; Ma, J.; Ding, T. Atomically thin two-dimensional organic-inorganic hybrid perovskites. *Science* **2015**, *349* (6255), 1518-1521.

(68) Guthrey, H.; Moseley, J. A review and perspective on cathodoluminescence analysis of halide perovskites. *Advanced Energy Materials* **2020**, *10* (26), 1903840.

(69) Yuan, F.; Zheng, X.; Johnston, A.; Wang, Y.-K.; Zhou, C.; Dong, Y.; Chen, B.; Chen, H.; Fan, J. Z.; Sharma, G. Color-pure red light-emitting diodes based on two-dimensional lead-free perovskites. *Science Advances* **2020**, *6* (42), eabb0253.

(70) Wang, K.; Wu, C.; Jiang, Y.; Yang, D.; Wang, K.; Priya, S. Distinct conducting layer edge states in two-dimensional (2D) halide perovskite. *Science Advances* **2019**, *5* (7), eaau3241. DOI: 10.1126/sciadv.aau3241.

(71) Kubicki, D. J.; Prochowicz, D.; Salager, E.; Rakhmatullin, A.; Grey, C. P.; Emsley, L.; Stranks, S. D. Local structure and dynamics in methylammonium, formamidinium, and cesium tin (II) mixed-halide perovskites from 119Sn solid-state NMR. *Journal of the American Chemical Society* **2020**, *142* (17), 7813-7826.

(72) Leijtens, T.; Prasanna, R.; Gold-Parker, A.; Toney, M. F.; McGehee, M. D. Mechanism of tin oxidation and stabilization by lead substitution in tin halide perovskites. *ACS Energy Letters* **2017**, *2* (9), 2159-2165.